Gu Xihui (Orcid ID: 0000-0002-1924-9282)

Li Jianfeng (Orcid ID: 0000-0002-9288-3415)

Ren Guoyu (Orcid ID: 0000-0002-9351-4179)

Contributions of global warming and urbanization to the intensification of human-perceived heatwaves over China

Dongdong Kong[1], Xihui Gu[1, 2, *], Jianfeng Li[2, *], Guoyu Ren[1, 3], Jianyu Liu[4]

1. Department of Atmospheric Science, School of Environmental Studies, China University of Geosciences, Wuhan, China;
2. Department of Geography, Hong Kong Baptist University, Hong Kong, China;
3. Laboratory for Climate Studies, National Climate Center, China Meteorological Administration, Beijing, China;
4. Hubei Key Laboratory of Critical Zone Evolution, School of Geography and Information Engineering, China University of Geosciences, Wuhan, China

* Corresponding authors: Xihui Gu (guxh@cug.edu.cn) and Jianfeng Li (jianfengli@hkbu.edu.hk)

Key points:

This article has been accepted for publication and undergone full peer review but has not been through the copyediting, typesetting, pagination and proofreading process which may lead to differences between this version and the Version of Record. Please cite this article as doi: 10.1029/2019JD032175

- The occurrence probability of HWs nearly doubled over recent decades, of which 72.9% was attributable to GHG and 21.9% to urbanization
- The occurrence probability of HWs will increase by 11.95 times at 3.5℃ warming, of which 91% is attributable to human-induced warming
- The occurrence probability of heatwaves varies by regions, with the highest sensitivity to human-induced warming in Southern China

Abstract Urbanization and global warming are the two major drivers of the warming environment in cities. The contributions of urbanization and global warming to the past occurrence of human-perceived heatwaves (HWs) over China are evaluated in this study. Both observations and model simulations show HWs have become more intensive, longer-lasting, and more frequent in recent decades. Urbanization and greenhouse gases contribute to 21.9% and 72.9% of the intensification of HWs, respectively. The occurrence probability of observed human-perceived HWs has doubled over 1961-2012 and is projected to be about 4.36/5.92 times under the 1.5/2℃ warming relative to the preindustrial level. At the 3.5℃ warming, the average duration of HWs is projected to increase to 43.63 days/year, and the occurrence probability is expected to increase by 11.95 times, 91% of which is attributable to human-induced warming. The highest sensitivity of the increases in HWs due to human-induced warming is in Southern China.

Plain Language Summary Both in-situ observations and model simulations show that the occurrence probability of human-perceived heatwaves (HWs) nearly doubled in China over recent decades, of which urbanization and greenhouse gases contribute to 21.9% and 72.9% of the intensification of HWs. When the China warming level reaches 3.5℃respective to the preindustrial period, the occurrence probability of HWs is expected to be 11.95-fold than that in the preindustrial period. The contribution of human-induced warming to the increase in

occurrence probability of HWs would be 91%. Southern China is the region where the intensification of HWs is most prominent due to human-induced warming. Increased adaptation and mitigation efforts are needed in China specifically Southern China to offset the increasing HWs due to urban expansion and anthropogenic activities.

Keywords: Human-perceived heatwaves; Global warming; Urbanization; Attributions; China

1. Introduction

Heatwaves (HWs) potentially pose threats on many different aspects of the society and ecosystems, such as public health, food security, energy production, and distribution, and ecosystem sustainability (Frölicher et al., 2018; He et al., 2018; McMichael et al., 2006; Yuan et al., 2016). Persistent HWs not only directly lead to heat-caused morbidity and mortality (e.g. heat stroke), but also indirectly raise the incidence of heat-related psychological and chronic diseases (e.g. insomnia, fatigue, cardiovascular and respiratory diseases) (Kang & Eltahir, 2018; Li et al., 2018; McMichael et al., 2006; Stott et al., 2004; Tan et al., 2007; Z. Xu et al., 2016). Rapid urbanization especially in the developing world over the recent decades exacerbates the warming of urban environment by urban heat island effects on one hand and raises the health risks in cities due to the fast-paced growth of urban population on the other hand (Manoli et al., 2019). As the most populated country of the world, China has experienced the fastest and most intensive urbanization over the recent decades, suggesting the non-neglectful impacts of urbanization on the intensification of HWs in Chinese cities despite global warming.

HWs in China have become more frequent and severe (Su & Dong, 2019), especially since the mid-1990s. Several record-breaking HW events attacked China in recent decades, such as the July-August 2013 HW event in eastern China and the 2015 summer HW event in western China (Su & Dong, 2019). The 2013 summer HW event was the hottest on records in eastern

China (Sun et al., 2014). This persistent HW event lasted for more than 30 days and the regionally averaged surface air temperature was 1.89°C above the 1961–90 climatology (Ma et al., 2017), causing 5758 cases of HW-related illness (Gu et al., 2016). Subsequently, the 2015 summer HW event registered the hottest summer in western China with the highest temperature of 47.7°C and the daily maximum temperature above 38°C covering an area of about 753,000 km^2 during 12 June – 10 August (Sun, Song, et al., 2016). Given the increasing threats of HWs, it is of great importance to understand and quantify the causes of the intensification of HWs.

Several studies have attributed the recorded HWs to anthropogenic forcing (Meehl et al., 2007; Rahmstorf & Coumou, 2011; Su & Dong, 2019; Sun et al., 2014; Xu et al., 2018). On the other hand, rapid urbanization alters the surface energy budget and results in higher temperature in urban areas than rural areas, i.e. urban heat island effects (Wang et al., 2017). Therefore, urbanization brings about additional increases in air temperature in cities on top of those induced by anthropogenic greenhouse gases forcing (GHG) (Zhang et al., 2015; Zhang et al., 2011). The impacts of urbanization on the observed HWs were not well considered in previous studies, which potentially caused the overestimation of the contribution of GHG forcing. This is particularly the case in China, as most of the stations from the meteorological observation network of China are located in urban or urbanizing areas, although urban areas only account for less than 5% of the land area in China (Ren et al., 2015). Thus, several recent studies suggested that urbanization contributes a third of observed warming in China (Ren et al., 2008; Sun, Zhang, et al., 2016; Zhang et al., 2011) and is a key contributor of the unprecedented HWs in eastern and southern China (Liao et al., 2018; Luo & Lau, 2017, 2018; J. Wang et al., 2017; Ye et al., 2018; Zhang et al., 2011).

Although it has been qualitatively proven that the observed intensification of HWs over China is the joint effects of global warming and urbanization (Luo & Lau, 2017; Su & Dong,

2019; Sun, et al., 2016), limited studies so far have been conducted to quantify the individual contributions of these two drivers to the changes in HWs. What's more, previous attribution researches mainly focus on the air temperature-based HW. But the heat index-based HW, also known as the human-perceived HW, has a direct link to the heat stress that human body really perceives (Li et al., 2018; Mora et al., 2017; Russo et al., 2017). In this study, we employ the optimal fingerprint method and the fraction of risk attributable method, two widely used "Detection and Attribution methods" (Allen & Stott, 2003; Allen & Tett, 1999; Fischer & Knutti, 2015), to analyze the attribution of changes in human-perceived HW characteristics, i.e. duration, maximum intensity, cumulative intensity, and frequency, to global warming and urbanization, and based on the attribution analysis to project the future progression of HWs.

2. Data and Methods

2.1 Site observations

Historical *in-situ* daily surface air mean temperature (T_{mean}) and daily relative humidity (*RH*) of 2,419 meteorological stations over the period of 1961-2012 were used in this study. The meteorological observations are obtained from the National Meteorological Information Center, China Meteorological Administration (CMA). The raw temperature and RH data were quality-controlled and homogenized by the method of Xu et al., (2013) in software RHtest (Wang & Feng, 2013) to eliminate non-climatic variations induced by changes in instrumentation, local site condition, environment, etc. (Vincent et al., 2012).

Similar as Liao et al., (2018), We classify 2,419 meteorological stations into urban and rural stations according to the dynamic land use/land cover (LULC) data, which is generated from Landsat TM/ETM+ images with a resolution of 30m, and is available at the Data Center for Resources and Environmental Sciences, Chinese Academy of Sciences (http://www.resdc.cn/data.aspx?DATAID=95). Those LULC data are only available in 1980,

1990, 1995, 2000, 2005, and 2010. Correspondingly, the researching period (1961-2012) is divided into 1961-1980, 1981-1990, 1991-1995, 1996-2000, 2001-2005, and 2006-2012, and each subperiod shares the same LULC data. A station is classified as urban if the percentage of buildup area of its corresponding 2-km circular buffer is greater than 33%. Otherwise, it is classified as a rural station. The spatial distribution of identified urban and rural stations in 1980, 1990, 1995, 2000, 2005, and 2010 is presented in Figure 1. There are 332 urban stations in 1980, and the number grows into 1,022 in 2010.

China is further divided into $5^{\circ} \times 5^{\circ}$ latitude-longitude grids to identify the urbanization effect (Liao et al., 2018; Sun, Zhang, et al., 2016). Only those $5^{\circ} \times 5^{\circ}$ grids with at least one rural and one urban station inside are considered. Finally, 39 grids are selected. The observational data in these selected $5^{\circ} \times 5^{\circ}$ grids have complete coverage over mainland China and can be matched to CMIP5 General Circulation Models (GCMs) outputs. In each grid cell, HW characteristics are first calculated for each station individually, and then the urban (rural) stations inside the grid cell are averaged to generate the grid-level urban (rural) HW characteristics (abbreviated as OBS_{urban} and OBS_{rural} respectively). Both urban and rural stations within the grid cell are averaged to get the grid-level HW characteristics over China (abbreviated as OBS_{whole}) (Liao et al., 2018).

2.2 Coupled Model Intercomparison Project Phase 5 (CMIP5) data

Responses of HWs to external forcings including historical forcing (anthropogenic and natural forcings, ALL), external natural forcing only (solar and volcanic combined, NAT), and greenhouse gases forcing only (GHG) are evaluated in this study based on the outputs of GCMs from the Coupled Model Intercomparison Project Phase 5 (CMIP5). The unforced preindustrial control (piControl) runs are used to quantify the internal variability. T_{mean} and specific humidity (q) of GCMs during 1961-2012 are analyzed (Table 1). For GCM ALL simulations ending in 2005, we extend them by corresponding Representative Concentration Pathway

(RCP) 4.5 simulations during 2006-2012, as the RCP4.5 simulations match the current economic developing path best (Sun, Zhang, et al., 2016). For NAT and GHG simulations, we only select simulations that cover the period of 1961-2012. RCP2.6 and RCP8.0 scenarios covering the end of the 21st century, are used to analyze the future progression of HWs. RCP2.6, RCP4.5 and RCP8.0 represent radiative forcings of +2.6, +4.5, and + 8.5 W/m2 in the year 2100 to preindustrial values, respectively. In this study, we only choose the first ensemble of the simulation runs ("r1i1p1") to conduct our analyses, so that all models have the same weight when we calculate the multi-model ensemble mean.

2.3 Definition of human-perceived HWs

Heat index (HI, in ℃), also known as the apparent temperature, has a direct link to the heat stress that human body really perceives *(Li et al., 2018; Mora et al., 2017; Russo et al., 2017)*. HI is employed to define HW events in this study, which is calculated by the Rothfusz regression (Li et al., 2018; Luo & Lau, 2018; Rothfusz & Headquarters, 1990):

$$\begin{aligned} \mathrm{HI} = & -8.784695 + 1.61139411\times \mathrm{T} - 2.338549\times \mathrm{RH} \\ & - 0.14611605\times \mathrm{T}\times \mathrm{RH} - 1.2308094\times 10^{-2}\times \mathrm{T}^2 \\ & - 1.6424828\times 10^{-2}\times \mathrm{RH}^2 + 2.211732\times 10^{-3}\times \mathrm{T}^2\times \mathrm{RH} \\ & + 7.2546\times 10^{-4}\times \mathrm{T}\times \mathrm{RH}^2 + 3.582\times 10^{-6}\times \mathrm{T}^2\times \mathrm{RH}^2 \end{aligned}, \quad (1)$$

where T is the land surface air temperature (in ℃) and RH is the relative humidity (in %). Further adjustments are applied to HI when RH < 13% and 26.7° < T < 44.4 °C, and when RH > 85% and 26.7 °C < T < 30.6 °C (Luo & Lau, 2018) (https://www.wpc.ncep.noaa.gov/html/heatindex_equationbody.html). Because only a few CMIP5 GCMs have daily RH simulation directly. RH is derived from actual specific humidity (q), and is equal to the ratio of q to saturated specific humidity (q_{sat}). Furthermore, q_{sat} is estimated by Tetens' formula (Buck, 1981):

$$\begin{aligned} q_{sat} &= 0.62197(e_w / (P_a - 0.378e_w)) \\ e_w &= 6.1121(1.0007+3.46*10^{-6}P_a)exp(\frac{17.502T}{240.97+T}) \end{aligned}, \quad (2)$$

where e_w is the land surface saturated vapor pressure, P_a is the land surface air pressure, Pa is treated as a constant value 1020 hPa in this study.

Human-perceived HWs are defined as days with HI > a specified threshold (hereafter, HWs in this study are referred to human-perceived HWs if without specific instruction). The thresholds are the percentiles of daily HI at each grid during the last 200 years of piControl simulations (Fischer & Knutti, 2015; Frölicher et al., 2018) in the future HWs analysis (Figures 6-11). When comes to historical HWs analysis in Figures 3-5, for fair comparison, both of the observed HWs and GCMs simulated HWs used the percentiles of daily HI during 1961-1990. Without special instruction, the threshold refers to the 99% quantile in this study. We also used other thresholds (e.g. 90%, 95%, 99.9% and 99.99%) to test the robustness of our study in Figure 8. The same piControl simulations over the last 200 years are also used to define the reference temperature relative to which warming level reaches. We further quantify the following HW characteristics, including maximum intensity (HWI, in units of ℃, maximum temperature anomaly with respect to a threshold over the HW period), duration (HWD, in units of days, number of days of temperature exceeding a threshold), cumulative intensity (HWCI, in units of ℃, mean intensity multiplied by duration), and frequency (HWF, the number of HW events of a year) (Figure 2).

2.4 Detection and attribution methods

The contribution of urbanization to increases in HWs is defined as the difference of trends in area-averaged time series of each HW characteristic between urban and rural areas (namely $\mathrm{Trend}_{urban} - \mathrm{Trend}_{rural}$). Afterward, the percentage of urbanization contribution is defined as Eq. 3 (Luo & Lau, 2018; Ren & Zhou, 2014). The contribution of urbanization to HW characteristics OBS_{whole} is quantified by Eq. 4.

$$RC_{urban} = \frac{Trend_{urban} - Trend_{rural}}{Trend_{urban}}, \qquad (3)$$

$$C_{urban} = Trend_{whole} \times RC_{urban}, \qquad (4)$$

where $Trend_{urban}$, $Trend_{rural}$ and $Trend_{whole}$ are linear trends of OBS_{urban}, OBS_{rural} and OBS_{whole} respectively.

The separate contributions of external forcing factors, i.e. ALL, GHG and NAT, to the increasing HWs are quantified by the optional fingerprinting method (Allen & Stott, 2003; Allen & Tett, 1999), which has been widely applied to detect anthropogenic contributions to changes in temperature, precipitation, soil moisture (Chen & Sun, 2017; Gu et al., 2019; Sun et al., 2016). This method assumes that *Y* (the observation signal) is the sum of scaled fingerprints *X* plus the internal variability:

$$\mathbf{y} = \sum_{i=1}^{m} \mathbf{x}_i \beta_i + v = \mathbf{X}\beta + v, \qquad (5)$$

where y is the rank-n vector of observations, the m columns of *X* are the climate model-simulated response patterns, and v is the regression residual or internal variability of y. The scaling factor β is the pattern-amplitude, and can be estimated by the ordinary least squares (OLS) method (Allen & Tett, 1999). A fingerprint signal is detectable if its scaling factor is positive and its 90% uncertainty range excludes zero. The fingerprint method used in this study is the same as employed in Gu et al., (2019). The description of this method is derived from there with minor modification. We conducted one-signal and two-signal detection and attribution analyses, respectively. One-signal analysis involving only one external forcing each time, shows whether a certain forcing is presented in the observations. Two-signal analysis including two external forcings (i.e. GHG and NAT) in *X*, can separate the responses of the two forcings (Wen et al., 2013).

In the fingerprint method, the attributable HW changes to external forcings can be quantified by Eq. 6.

$$\hat{C}_x = \beta_x \times \mathrm{trend}_x \times \mathrm{n}, \qquad (6)$$

where $\hat{C}_x$ is the estimated attributable changes to external forcing (x, i.e. GHG, NAT and ALL forcings in this study), β_x is the regression coefficient of corresponding external forcing estimated in the optional fingerprinting method, trend_x is the linear trend of external forcing over 1961-2012, and n is the length of year over 1961-2012 (i.e. 52). In the fingerprinting method, the urbanization effects are not considered and the observed HWs from rural stations is regressed on external forcings. Similar as Yuan et al. (2018), to reconcile the contributions of external forcings to observed HW characteristics averaged by both urban and rural stations over China (OBS_{whole}), we further adjust the contributions of external forcings according to the contributions of urbanization:

$$coef_{adj} = \frac{C_{ALL}}{\hat{C}_{ALL}} = \frac{C_{whole} \times (1 - RC_{urban})}{\hat{C}_{ALL}}, (7)$$

$$\hat{C}_{x,adj} = \hat{C}_x \times coef_{adj}, (8)$$

where $\hat{C}_{ALL}$ is the estimated attributable changes to ALL forcing in Eq. 6, C_{whole} is the change in OBS_{whole} over 1961-2012 (i.e. $C_{whole} = Trend_{whole} \times n$), RC_{urban} is the contribution of urbanization, and $coef_{adj}$ is the adjustment coefficient which is used to adjust the attributions of external forcing (i.e. $\hat{C}_x$, the attributions of GHG, NAT, and ALL forcings estimated in Eq. 6).

Based on RCP simulations, the comprehensive influence of anthropogenic drivers (ozone depletion, land-use change, aerosols, and greenhouse gases) on future HWs progression are investigated by two metrics, i.e. the probability ratio (PR) and fraction of attributable risk (FAR), which have been widely used to attribute climate extreme changes (Allen, 2003; Chen & Sun, 2017; Fischer & Knutti, 2015; Frölicher et al., 2018; Stott et al., 2004).

$$\mathrm{PR} = \frac{P_1}{P_0}, FAR = 1 - \frac{1}{\mathrm{PR}} = 1 - \frac{P_0}{P_1}, \qquad (9)$$

where P_1 is the probability of HW events at any given point of time (e.g. today) and P_0 is the probability of HW events during preindustrial period. PR represents the probability that a HW

event has changed. FAR quantifies the fraction of a HW event attributable to human-induced warming (Allen, 2003; Chen & Sun, 2017; Frölicher et al., 2018).

3. Results

Figure 3 shows temporal changes in annual area-averaged HW indices of *in-situ* observations and ALL forcing-based GCM simulations during 1961-2012. The magnitudes of GCM-simulated changes are consistent with those of observed HWs. The observed HWD, HWF and PR are in the 5%-95% interval of the GCM-simulated (Figures 3a, 3b and 3e), indicating that GCMs can adequately reproduce the observed HW variations. Being slightly overestimated, the GCMs simulated HWI and HWCI are less reliable than HWD, HWF and PR (Figures 3c-3d). The five GCM-simulated HW indices in present-day 1991-2012 almost double from that in earlier period 1961-1990. Over 1961-2012, the modeled HWD, HWF, HWI, HWCI, and PR increase significantly ($p < 0.01$) by 1.10±0.46 day/decade, 0.42±0.17 times/year/decade, 0.18±0.08 ℃/decade, 1.47±0.57 ℃/decade, and 0.30±0.13/decade, respectively, implying that the signal of increasing HWs is strong enough to be detected from the internal noise.

With the warming temperature, HWs become significantly longer, stronger and more frequent in both urban and rural areas ($p < 0.01$), and the slopes of increases in all HW indices are faster in urban areas than those in rural areas. Specifically, over these 52 years, annual HWD, HWF, HWI and HWCI of observed urban HWs increase by 4.0 days (90% confidence interval, 2.7-5.4), 1.5 times/year (1.0-2.0), 0.77℃ (0.28-1.31), and 5.48℃ (3.53-7.94), respectively, while these values for observed rural compound HWs are 3.1 days (1.8-4.4), 1.2 times/year (0.7-1.7), 0.53℃ (0.10-1.03), and 3.90℃ (2.00-5.98), respectively. Additionally, the occurrence probability of HWs increases by 0.24±0.04/decade in urban areas, and the value for rural areas is 0.19±0.04/decade (Figure 3e).

We further quantify the contribution of urbanization to the changes in observed HWs (Figure 4). For HWD, HWF, HWI, HWCI and PR of compound HWs over 1961-2012, attributable changes to urbanization are 0.77 day, 0.24 times/year, 0.20℃, 1.40 ℃, and 0.21 respectively, which account for 22.5%, 17.8%, 31.7%, 29.6 % and 21.9% of total changes. The magnitude of the urbanization contribution is in agreement with previous studies. For example, Ren et al., (2015) found that urbanization contributes 24.9% of the surface air temperature warming trend in China during 1961-2004. Sun et al., (2016) reported that urbanization contributes 1/3 of the observed warming in China during 1961-2013. In comparison, urbanization contributes 31.7 for HWI in our study. Luo & Lau (2018) found that urbanization contributes 24.3% to the frequency of extreme heat stress day over eastern China. While from eastern China to western China where the climate becomes arid, the contribution of urbanization to the increasing HWs becomes smaller and even negative (Liao et al., 2018). Hence, in our study, the contribution of urbanization to China HWF (i.e. 17.8%) is slightly smaller than that of Luo & Lau (2018).

To isolate urbanization effect from external forcings, observed HWs in rural stations were treated as the response variable (i.e. **y** in Eq. 5) to regress for individual forcings (i.e. ALL, GHG, or NAT). The scaling factors of ALL and GHG are positive and their 90% confidence intervals are above zero for HWD, HWF, HWI, and PR, indicating that the fingerprint of these external forcings can be detected in observed HWs (left panel of Figure 4). The scaling factors of ALL forcing are almost equal to 1, which again indicates consistency between site observations and the model simulated response (Wan et al., 2015). However, the scaling factor ranges of GHG forcing are only half of ALL forcing, suggesting that the multimodel ensemble HWs in China response to GHG forcing are generally overestimated. This is consistent with other studies, such as Wen et al. (2013) and Sun et al. (2016). However, when comes to HWCI, ALL and GHG are only detectable under the 85% confidence level. This may be induced by

that GCMs performs worse in simulating HW intensity and cumulative intensity than in simulating HW duration and frequency (Figures 3c-3d), which introduce extra uncertainty in the fingerprint regression.

As the changes in observed HW characteristics can be influenced by multiple forcings (Chen & Sun, 2017; Gu et al., 2019; Wen et al., 2013), two-signal analysis is applied to detect whether GHG forcing can be separated from NAT (Figure 5). Consistent with one-signal analysis, except for HWI, the GHG scaling factors are still significantly greater than zero for HWD, HWF and PR. These results suggest that GHG signal is still detectable for the observed HWD, HWF and PR over China when separating the influence of NAT.

Attributable changes to these external forcings are quantified by computing trends in ALL, GHG and NAT and then multiplying them by the corresponding scaling factors (Figure 4, right panels). "OBS" in Figure 4 indicates changes in observed HW characteristics averaged by both urban and rural stations (OBS_{whole}) over 1961-2012. The attributions of external forcings are estimated based on observed rural HWs, and thus are adjusted according to the contributions of urbanization to make them comparable to the observed HWs in the whole China (OBS_{whole}) (Eq. 8). For OBS_{whole} HWs over 1961-2012, the HWD, HWF, HWI, HWCI and PR increase by 3.4 days (2.2-4.8), 1.3 times/year (0.8-1.8), 0.64℃ (0.21-1.12), 4.72℃ (2.75-6.88) and 0.96 (0.61-1.34) respectively, of which 72.4%, 74.1%, 68.7%, 60.7%, and 72.9% are attributable to GHG forcing. Our results of contributions of these external forcings are consistently lower than those detected in previous studies without considering the urbanization effects. For example, Wen et al. (2013) attributed 89% and 95% of observed annual warmest day and night temperature to GHG forcing, while the GHG attributes 68.7% for HWI in our study.

We further extend the time evolution of HW characteristics to the future by the RCP2.6 and RCP8.5 scenarios (Figure 6). The difference of HW characteristics under RCP2.6 and RCP8.5 is measurable after the 2030s. Under RCP2.6, HW characteristics reach the maximum

in the 2050s, and then become stable afterward. Under RCP8.5, HW characteristics increase exponentially over the 21st century and are substantially higher than those under RCP2.6. For example, at the end of the 21st century, mean HWD, HWF, HWI, HWCI and PR of compound HWs over China are projected to be 78.1 days, 10.0 times/year, 11.1℃, 365.7℃ and 21.43 under RCP8.5, respectively, while the values are 23.5 days, 7.0 times/year, 4.5℃, 45.2℃ and 6.43 under RCP2.6, respectively. These results imply a strong connection between human-induced warming and increases in HWs.

We also used the RCP scenarios to estimate the response of future HW characteristics to different level warmings and the overall contribution of global warming and urbanization to the future increasing HWs by FAR (Figure 7). For HWs exceeding the 99th percentile of the preindustrial period, the mean duration of HWs in the preindustrial period is 4.0 days (3.2-5.5), the mean intensity is up to 2.0℃ (1.5-2.8), and the cumulative intensity is 6.6℃ (4.6-9.0). On average, the HWs are projected to last for 43.6 days (32.3-54.5) and have a cumulative intensity of 117.3℃ (80.4-146.2) under 3.5℃ warming (Table 2). Meanwhile, compared to the preindustrial level, the occurrence probability of observed HWs doubled over 1961-2012, and is projected to be 4.36-fold (3.03-5.70), 5.92-fold (4.05-7.95) and 11.95-fold (8.84-14.94) under 1.5℃, 2℃ and 3.5 ℃ warming levels, respectively (Table 3). Because of the large increase in the occurrence probability with human-induced warming, the simulated FAR—that is, the human contribution to the probability of an event—reaches 91% at 3.5℃ warming level. When higher quantiles are taken as the thresholds to define HWs, larger occurrence probability with warming is estimated (Figure 8). For example, at the 3.5℃ warming level, PR defined by the 99th percentile is about 11.95 (8.84-14.94), and it is raised to 300.22 (106.00-486.78) when the 99.99th percentile is taken as the threshold.

RCP scenarios include the natural forcings (e.g. solar changes and volcanic eruptions) and anthropogenic forcings (e.g. aerosols, ozone depletion, land cover changes and GHG) and are

dominated by GHG at the end of 21st century (Marvel et al., 2019). RCP scenarios take land cover changes into account. Known that urbanization is a part of land cover changes, hence, RCP scenarios can simulate the urbanization effect. But due to the coarse resolution in the GCMs, the ability in simulating the urbanization effect in GCMs might be limited. In the results of fingerprint regression (Figure 4), we know that GHG is the dominant factor in the increasing HWs, which contributes to 72.9% of the increasing HWs in China during 1961-2012. Hence, the weak ability of simulating urbanization effect in GCMs will have a relatively small influence on future HW characteristics. On the other hand, in Figure 7, we can conclude that the increase of HW characteristics under different warming levels is independent of developing path (i.e. RCP2.6 or RCP8.5), and only the extent of temperature warming matters. Even though GCMs have limited ability in simulating urbanization impact, it only impacts the reaching time of certain warming level and will not alert the correlation of the increase of HW characteristics and warming level, and will not change the overall contributions of anthropogenic forcings to the increasing HWs at certain warming level.

Although the occurrence probability of HWs is projected to increase across China, the changes in occurrence likelihood vary in spatial (Figures 9-10). HWs of low-latitude regions are more sensitive to human-induced warming than the high-latitude regions. Because the increase of PR in low-latitude regions is substantially higher than that of high-latitude regions under the same warming level (Figure 9). We selected six representative regions which are across different latitudes and have a distinguished pattern of PR and FAR responding to different warming levels (Figures 9-10), and presented the evolution of simulated changes of PR and FAR under different levels of warming (Figure 11). The occurrence likelihood of HWs in those six representative regions (A) Northeastern China, (B) XinJiang, (C) Beijing-Tianjin-Hebei, (D) XiZang, (E) Central China, (F) Southern China are about 1.61, 1.68, 1.91, 2.71, 2.85 and 4.32 respectively at the present-day warming. Those numbers grow into 5.85, 6.62,

8.24, 12.2, 13.4 and 29.9 for the same regions at the 3.5℃ warming level (Figure 11a). Meanwhile, 79%, 83%, 86%, 91%, 92% and 97% of the HW changes in those regions can be attributed to human-induced warming at the 3.5℃ warming level (Figure 11b). Southern China is the region most sensitive to the increasing temperature (Figures 9d and 10d), where the occurrence likelihood of HWs will be 29.9-fold as the preindustrial period at the 3.5℃ warming level. The HWs in northern China (especially for Northeastern China) is relatively less sensitive to the impacts of human-induced warming, where the changes in PR are mainly in the range of [1, 2] (Figure 9a) and less than 6% of the changes are attributed to human-induced warming at the present-day warming (Figure 10a). Even so, when the temperature increases to 3.5 ℃, the PR in Northeastern China would increase to 5.85 and the contribution of human-induced warming would increase to 79.0%. As human activities become stronger, essentially all HWs over China are due to human-induced warming at 3.5 ℃ warming level (Figures 10 and 11b).

4. Conclusions

Stronger, longer and more frequent human-perceived HWs are observed in China over the past five decades (i.e. 1961-2012). The duration, maximum intensity, cumulative intensity, and frequency of HWs show significantly increasing trends ($p < 0.01$), while the magnitudes of increases vary obviously between urban and rural areas. The increase in occurrence probability of HWs is higher in urban areas than in rural areas (i.e. 0.24±0.04/decade vs 0.19±0.04/decade). Quantitative attribution analysis shows that urbanization contributes to 17.8%-31.7% (with an average 23.4%) of the increases in HWs over China, which is in line with the consensus (about 20%-30%) reached by previous studies (e.g. Luo & Lau, 2018; Ren et al., 2015; Sun, Zhang, et al., 2016).

Besides the impacts of urbanization, anthropogenic GHG forcing is the dominant factor controlling the increases of HWs over China. Based on the acceptable ability of CMIP5 GCMs in reproducing changes in HWs, our detection and attribution analyses show that the GHG signal is detectable (in the confidence level of 90%) in the increases of observed HWs. 69% (60.7-74.1%) of observed increases in HWs can be explained by GHG forcing, validating that anthropogenic climate change is the major driver of the increases in the occurrence likelihood of HWs over China in the recent decades.

As warming is expected to continue in the future, the contributable fraction of human-induced warming to the increases of HWs is expected to increase remarkably. At the 3.5℃ warming level, the occurrence likelihood of HWs exceeding the 99% quantile would increase to 11.95 times of that in the piControl runs, and human-induced warming contributes to 91% of the increases. The occurrence likelihood of extreme HWs exceeding the 99.99% quantile is projected to increase at a more substantial rate. The likelihood is expected to be 300.22 times of that in the piControl runs, and almost all of the increase is attributed to human-induced warming at the 3.5℃ warming level. The responses of HWs to human-induced warming vary by region over China, and the increases in the occurrence probability of HWs in Southern China are the most sensitive to future warming compared to other regions.

Acknowledgments

This study was supported by the National Key R&D Program of China (Grant 2018YFA0605603), National Natural Science Foundation of China (Grant Nos. 41901041 and U1911205), the Strategic Priority Research Program Grant of the Chinese Academy of Sciences (Grant XDA19070402), the grants from the Research Grants Council of the Hong Kong Special Administrative Region, China (Projects HKBU22301916 and HKBU12302518), the Fundamental Research Funds for the Central Universities, China University of Geosciences

(Wuhan) (grants CUG180614 and CUGCJ1702). We acknowledge the World Climate Research Programme's Working Group on Coupled Modeling, which is responsible for CMIP5. Mean daily surface air temperature and specific humidity of CMIP5 GCMs are available at the Lawrence Livermore National Laboratory website (https://esgf-node.llnl.gov/search/cmip5/). We acknowledge the China Meteorological Data Service Center which provides the observed daily temperature in a Chinese web site (http://data.cma.cn/). We also acknowledge the Data Center for Resources and Environmental Sciences, Chinese Academy of Sciences which provides the dynamic LULC data (http://www.resdc.cn/data.aspx?DATAID=95). Because we are not authorized to share original observed data, we make all the processed data including heatwave indices in each station available at https://doi.org/10.5281/zenodo.3553156.

References

Allen, M. (2003). Liability for climate change. *Nature*, *421*(6926), 891–892. https://doi.org/10.1038/421891a

Allen, M. R., & Stott, P. A. (2003). Estimating signal amplitudes in optimal fingerprinting, part I: Theory. *Climate Dynamics*, *21*(5–6), 477–491. https://doi.org/10.1007/s00382-003-0313-9

Allen, M. R., & Tett, S. F. B. (1999). Checking for model consistency in optimal fingerprinting. *Climate Dynamics*, *15*(6), 419–434. https://doi.org/10.1007/s003820050291

Buck, A. L. (1981). New equations for computing vapour pressure and enhancement factor. *Journal of Applied Meteorology*. https://doi.org/10.1175/1520-0450(1981)0202.0.CO;2

Chen, H., & Sun, J. (2017). Contribution of human influence to increased daily precipitation extremes over China. *Geophysical Research Letters*, *44*(5), 2436–2444. https://doi.org/10.1002/2016GL072439

Fischer, E. M., & Knutti, R. (2015). Anthropogenic contribution to global occurrence of heavy-precipitation and high-temperature extremes. *Nature Climate Change*, *5*(6), 560–564. https://doi.org/10.1038/nclimate2617

Frölicher, T. L., Fischer, E. M., & Gruber, N. (2018). Marine heatwaves under global warming. *Nature*, *560*(7718), 360–364. https://doi.org/10.1038/s41586-018-0383-9

Gu, S., Huang, C., Bai, L., Chu, C., & Liu, Q. (2016). Heat-related illness in China, summer of 2013. *International Journal of Biometeorology*, *60*(1), 131–137. https://doi.org/10.1007/s00484-015-1011-0

Gu, X., Zhang, Q., Li, J., Singh, V. P., Liu, J., Sun, P., & Cheng, C. (2019). Attribution of Global Soil Moisture Drying to Human Activities: A Quantitative Viewpoint. *Geophysical Research Letters*, *46*(5), 2573–2582. https://doi.org/10.1029/2018GL080768

He, L., Cleverly, J., Wang, B., Jin, N., Mi, C., Liu, D. L., & Yu, Q. (2018). Multi-model ensemble projections of future extreme heat stress on rice across southern China. *Theoretical and Applied Climatology*, *133*(3–4), 1107–1118. https://doi.org/10.1007/s00704-017-2240-4

Kang, S., & Eltahir, E. A. B. B. (2018). North China Plain threatened by deadly heatwaves due to climate change and irrigation. *Nature Communications*, *9*(1), 1–9. https://doi.org/10.1038/s41467-018-05252-y

Li, J., Chen, Y. D., Gan, T. Y., & Lau, N. C. (2018). *Elevated increases in human-perceived temperature under climate warming*. *Nature Climate Change* (Vol. 8). Springer US. https://doi.org/10.1038/s41558-017-0036-2

Liao, W., Liu, X., Li, D., Luo, M., Wang, D., Wang, S., et al. (2018). Stronger Contributions of Urbanization to Heat Wave Trends in Wet Climates. *Geophysical Research Letters*, *45*(20), 11,310-11,317. https://doi.org/10.1029/2018GL079679

Luo, M., & Lau, N.-C. (2017). Heat Waves in Southern China: Synoptic Behavior, Long-Term Change, and Urbanization Effects. *Journal of Climate*, *30*(2), 703–720. https://doi.org/10.1175/JCLI-D-16-0269.1

Luo, M., & Lau, N.-C. (2018). Increasing heat stress in urban areas of eastern China: Acceleration by urbanization. *Geophysical Research Letters*. https://doi.org/10.1029/2018GL080306

Ma, S., Zhou, T., Stone, D. A., Angélil, O., & Shiogama, H. (2017). Attribution of the July-August 2013 heat event in Central and Eastern China to anthropogenic greenhouse gas emissions. *Environmental Research Letters*, *12*(5). https://doi.org/10.1088/1748-9326/aa69d2

Marvel, K., Cook, B. I., Bonfils, C. J. W., Durack, P. J., Smerdon, J. E., & Williams, A. P. (2019). Twentieth-century hydroclimate changes consistent with human influence. *Nature*, *569*(7754), 59–65. https://doi.org/10.1038/s41586-019-1149-8

McMichael, A. J., Woodruff, R. E., & Hales, S. (2006). Climate change and human health: Present and future risks. *Lancet*, *367*(9513), 859–869. https://doi.org/10.1016/S0140-6736(06)68079-3

Meehl, G. A., Arblaster, J. M., & Tebaldi, C. (2007). Contributions of natural and anthropogenic forcing to changes in temperature extremes over the United States. *Geophysical Research Letters*, *34*(19), 1–5. https://doi.org/10.1029/2007GL030948

Mora, C., Dousset, B., Caldwell, I. R., Powell, F. E., Geronimo, R. C., Bielecki, C. R., et al. (2017). Global risk of deadly heat. *Nature Climate Change*, *7*(7), 501–506. https://doi.org/10.1038/nclimate3322

Rahmstorf, S., & Coumou, D. (2011). Increase of extreme events in a warming world. *Proceedings of the National Academy of Sciences*, *108*(44), 17905–17909. https://doi.org/10.1073/pnas.1101766108

Ren, G., Li, J., Ren, Y., Chu, Z., Zhang, A., Zhou, Y., et al. (2015). An Integrated Procedure to Determine a Reference Station Network for Evaluating and Adjusting Urban Bias in

Surface Air Temperature Data. *Journal of Applied Meteorology and Climatology*, *54*(6), 1248–1266. https://doi.org/10.1175/JAMC-D-14-0295.1

Ren, G. Y., Zhou, Y. Q., Chu, Z. Y., Zhou, J. X., Zhang, A. Y., Gou, J., & Liu, X. F. (2008). Urbanization effects on observed surface air temperature trends in north China. *Journal of Climate*, *21*(6), 1333–1348. https://doi.org/10.1175/2007JCLI1348.1

Rothfusz, L. P., & Headquarters, N. W. S. S. R. (1990). The heat index equation (or, more than you ever wanted to know about heat index). *Fort Worth, Texas: National Oceanic and Atmospheric Administration, National Weather Service, Office of Meteorology*, *9023*.

Russo, S., Sillmann, J., & Sterl, A. (2017). Humid heat waves at different warming levels. *Scientific Reports*, *7*(1), 1–7. https://doi.org/10.1038/s41598-017-07536-7

Stott, P. A., Stone, D. A., & Allen, M. R. (2004). Human contribution to the European heatwave of 2003. *Nature*, *432*(7017), 610–614. https://doi.org/10.1038/nature03089

Su, Q., & Dong, B. W. (2019). Recent Decadal Changes in Heat Waves over China: Drivers and Mechanisms. *Journal of Climate*, *32*(14), 4215–4234. https://doi.org/10.1175/Jcli-D-18-0479.1

Sun, Y., Zhang, X., Zwiers, F. W., Song, L., Wan, H., Hu, T., et al. (2014). Rapid increase in the risk of extreme summer heat in Eastern China. *Nature Climate Change*, *4*(12), 1082–1085. https://doi.org/10.1038/nclimate2410

Sun, Y., Song, L., Yin, H., Zhang, X., Stott, P., Zhou, B., & Hu, T. (2016). 20. Human influence on the 2015 extreme high temperature events in Western China. *Bulletin of the American Meteorological Society*, *97*(12), S102–S106. https://doi.org/10.1175/BAMS-D-16-0158.1

Sun, Y., Zhang, X., Ren, G., Zwiers, F. W., & Hu, T. (2016). Contribution of urbanization to warming in China. *Nature Climate Change*, *6*(7), 706–709. https://doi.org/10.1038/nclimate2956

Tan, J., Zheng, Y., Song, G., Kalkstein, L. S., Kalkstein, A. J., & Tang, X. (2007). Heat wave impacts on mortality in Shanghai, 1998 and 2003. *International Journal of Biometeorology*, *51*(3), 193–200. https://doi.org/10.1007/s00484-006-0058-3

Vincent, L. A., Wang, X. L., Milewska, E. J., Wan, H., Yang, F., & Swail, V. (2012). A second generation of homogenized Canadian monthly surface air temperature for climate trend analysis. *Journal of Geophysical Research Atmospheres*, *117*(17), 1–13. https://doi.org/10.1029/2012JD017859

Wan, H., Zhang, X., Zwiers, F., & Min, S. K. (2015). Attributing northern high-latitude precipitation change over the period 1966–2005 to human influence. *Climate Dynamics*, *45*(7–8), 1713–1726. https://doi.org/10.1007/s00382-014-2423-y

Wang, J., Yan, Z., Quan, X. W., & Feng, J. (2017). Urban warming in the 2013 summer heat wave in eastern China. *Climate Dynamics*, *48*(9–10), 3015–3033. https://doi.org/10.1007/s00382-016-3248-7

Wang, X. L., & Feng, Y. (2013). RHtests V4 User Manual. *Climate Research Division, Atmospheric Science and Technology Directorate, Science and Technology Branch, Environment Canada*. Retrieved from http://etccdi.pacificclimate.org/software.shtml

Wen, Q. H., Zhang, X., Xu, Y., & Wang, B. (2013). Detecting human influence on extreme temperatures in China. *Geophysical Research Letters*, *40*(6), 1171–1176. https://doi.org/10.1002/grl.50285

Xu, W., Li, Q., Wang, X. L., Yang, S., Cao, L., & Feng, Y. (2013). Homogenization of Chinese daily surface air temperatures and analysis of trends in the extreme temperature indices. *Journal of Geophysical Research Atmospheres*, *118*(17), 9708–9720. https://doi.org/10.1002/jgrd.50791

Xu, Y., Lamarque, J. F., & Sanderson, B. M. (2018). The importance of aerosol scenarios in projections of future heat extremes. *Climatic Change*, *146*(3–4), 393–406. https://doi.org/10.1007/s10584-015-1565-1

Xu, Z., FitzGerald, G., Guo, Y., Jalaludin, B., & Tong, S. (2016). Impact of heatwave on mortality under different heatwave definitions: A systematic review and meta-analysis. *Environment International*, *89–90*, 193–203. https://doi.org/10.1016/j.envint.2016.02.007

Ye, H., Huang, Z., Huang, L., Lin, L., & Luo, M. (2018). Effects of urbanization on increasing heat risks in South China. *International Journal of Climatology*, *38*(15), 5551–5562. https://doi.org/10.1002/joc.5747

Yuan, W., Cai, W., Chen, Y., Liu, S. S. S. S. S., Dong, W., Zhang, H., et al. (2016). Severe summer heatwave and drought strongly reduced carbon uptake in Southern China. *Scientific Reports*, *6*(January 2015), 1–12. https://doi.org/10.1038/srep18813

Zhang, L, Ren, G. Y., & Ren, Y. Y. (2015). Identification of urban effect on a single extreme high temperature event. *Climatic and Environmental Research (in Chinese)*, *20*(2), 167–176.

Zhang, Lei, Ren, G.-Y., Liu, J., Zhou, Y.-Q., Ren, Y.-Y., Zhang, A.-Y., & Feng, Y.-W. (2011). Urban effect on trends of extreme temperature indices at Beijing Meteorological Station. *Diqiu Wuli Xuebao*, *54*(5), 1150–1159.

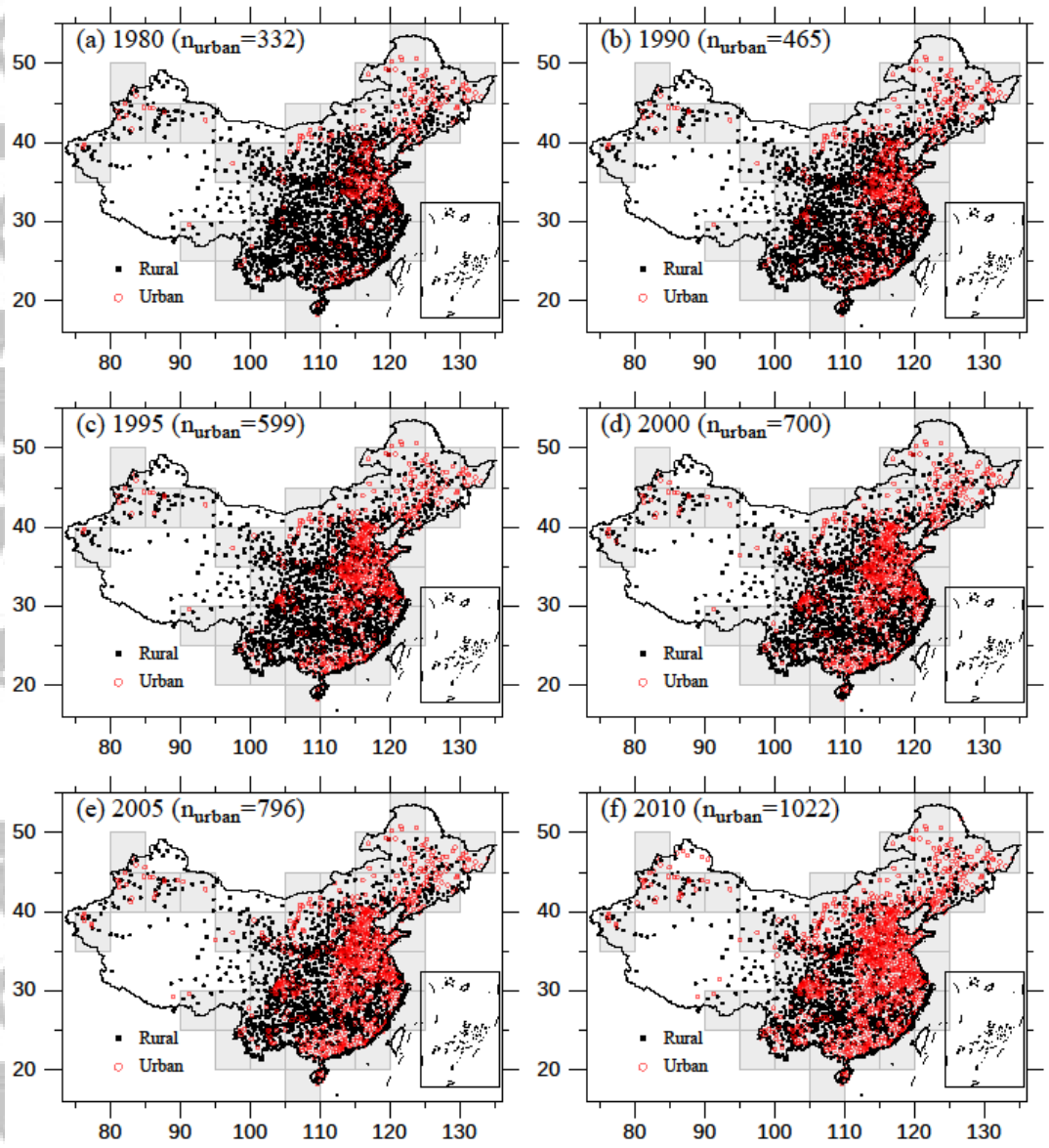

Figure 1. The distribution of rural and urban meteorological stations in different years. The grey grids are the selected $5^{\circ} \times 5^{\circ}$ grids which include at least one rural and one urban station.

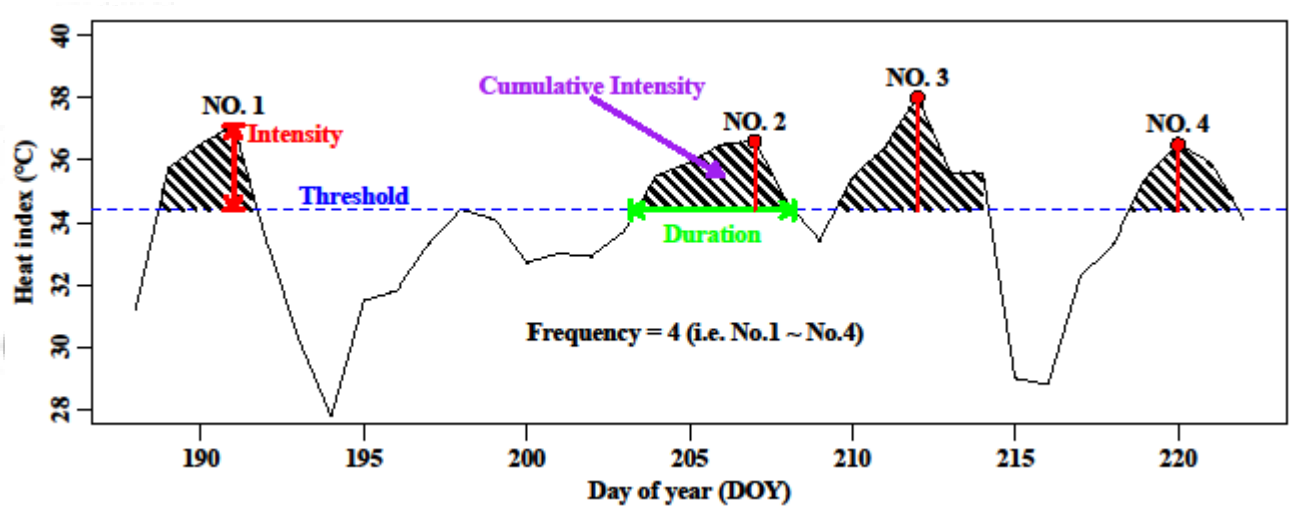

Figure 2. Delineation of human-perceived HW characteristics in this study. Hereafter, HWs are refered to human-perceived HWs if without specific instruction. HWs are identified as days with daily HI exceeding a specified threshold for successive days. Intensity (HWI) is the difference between the peak HI and the threshold. Duration (HWD) corresponds to the length of a HW cluster in days. Cumulative intensity (HWCI) is defined as the sum of the differences between the HI and the threshold over the HW period. Frequency (HWF) is the number of clusters a year.

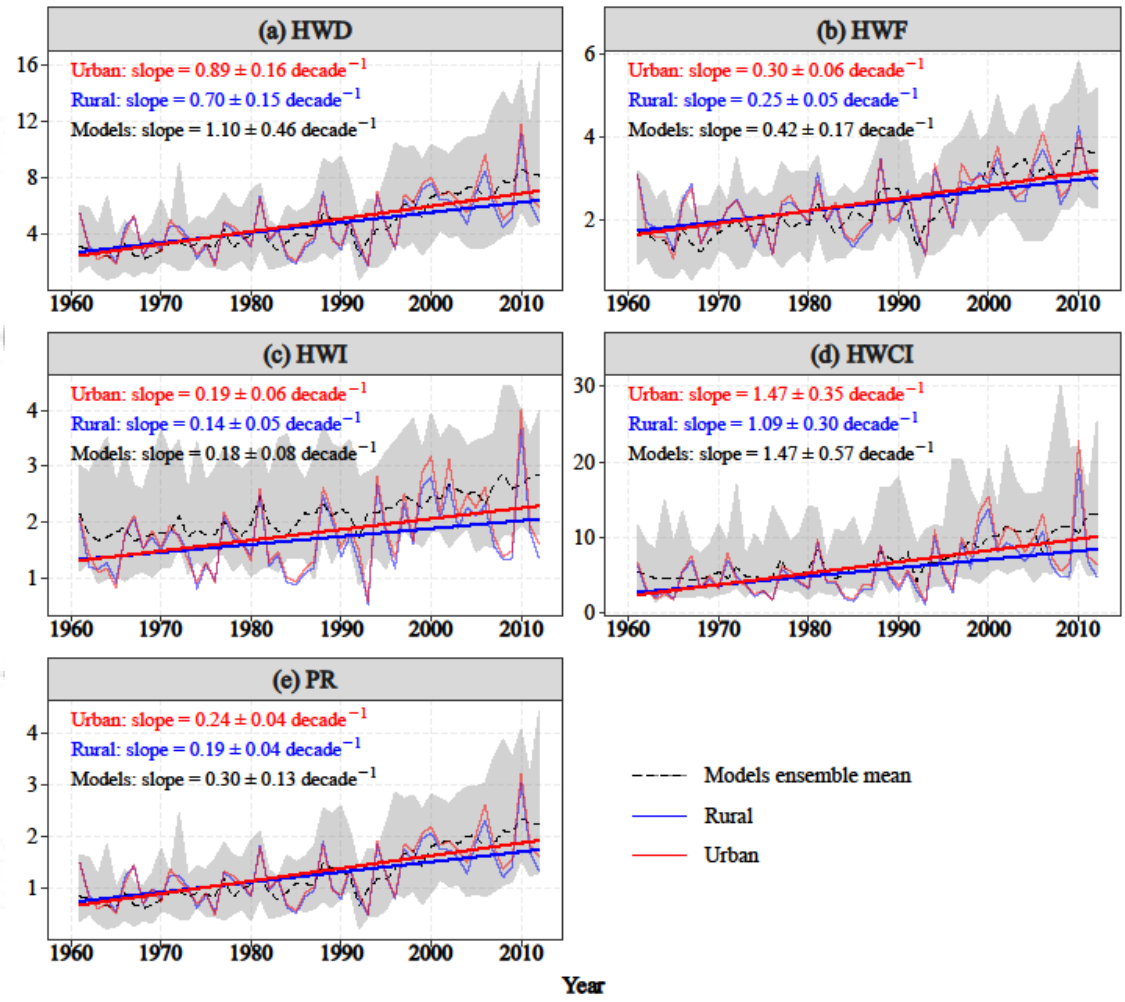

Figure 3. Temporal changes of (a) HWD, (b) HWF, (c) HWI, (d) HWCI, and (e) PR of observed and ALL simulated HW over the period of 1961-2012. HW is defined as days with HI > the 99% quantile of daily HI over the period of 1961-1990 for ALL simulations. The black dash line represents the multi-model ensemble mean. The grey shading shows the 5%-95% interval of the CMIP5 models. Blue (red) bold line is the linear trend of China area-weighted average of grid-level OBS_{rural} (OBS_{urban}). For "Urban" and "Rural", slope uncertainties are estimated as the standard deviation of 1000-times bootstrapping samplings. For "Models", slope uncertainties are estimated as standard deviation among multiple CMIP5 models.

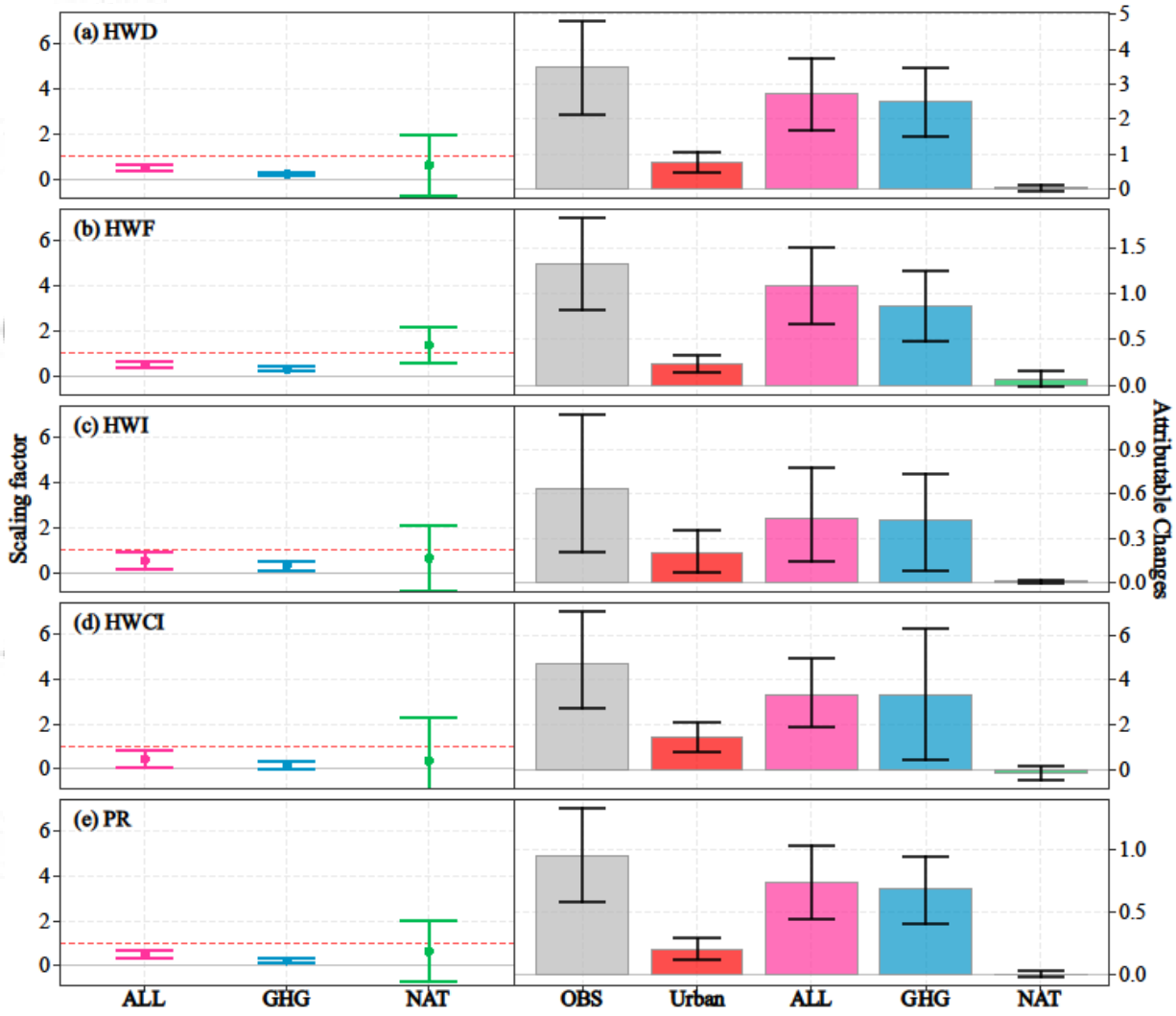

Figure 4. The best estimated one-signal scaling factors by OLS fingerprint method (left) and attributable changes (right) of area-weighted OBSwhole HW characteristics over the period of 1961-2012. "OBS" indicates changes in observed HW characteristics averaged by both urban and rural stations (OBS_{whole}) over 1961-2012. Attributable changes to ALL are from the one-signal analysis, and to GHG and NAT are from the two-signal analysis. Error bars indicate their corresponding 5-95% uncertainty intervals for each signal. For "OBS" and "Urban", uncertainties are estimated as 5-95% intervals of 1000-times bootstrapping samplings.

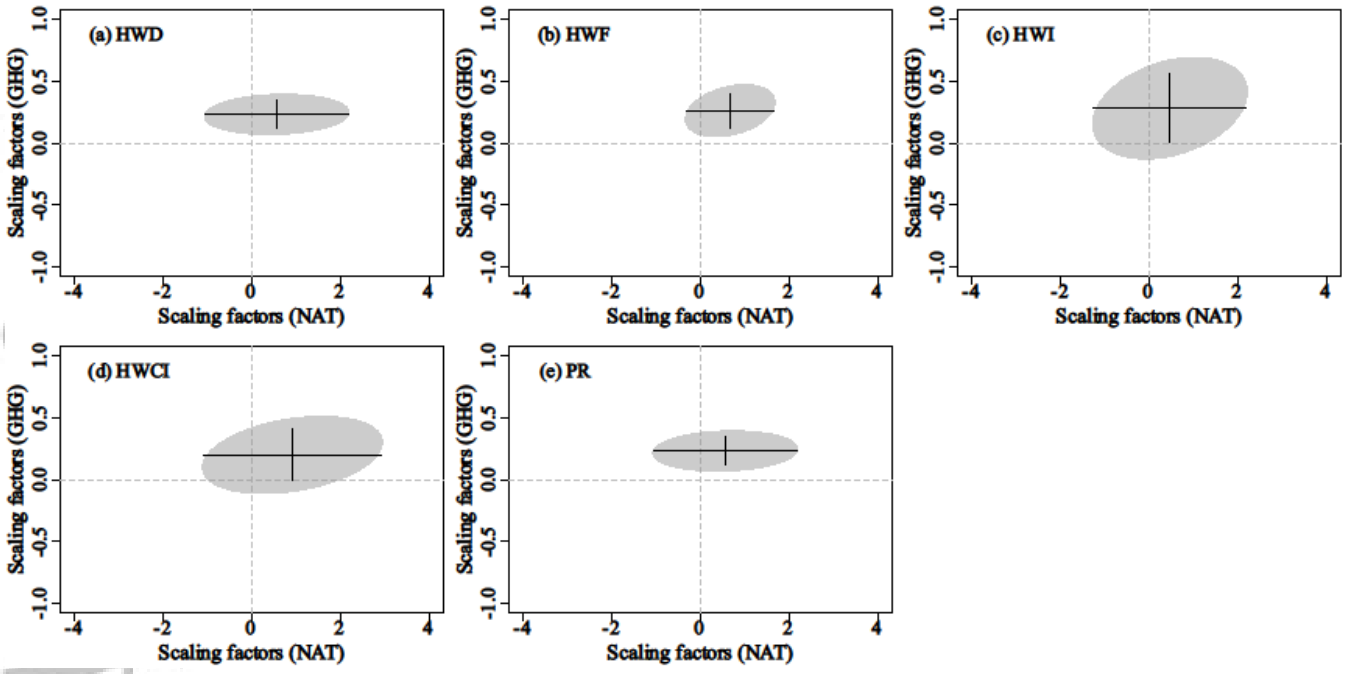

Figure 5. Two-signal scaling factors for HW changes from the OLS method and corresponding 5-95% confident intervals. In each panel, the shadows are the 5-95% joint confidence intervals of scaling factors.

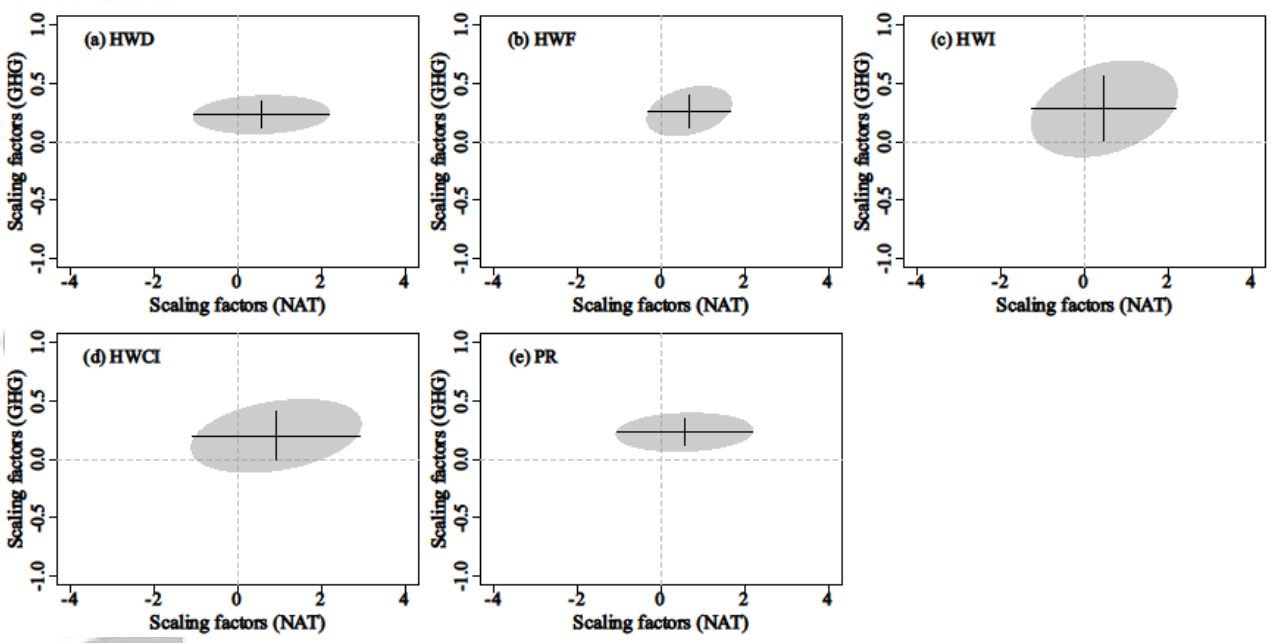

Figure 6. Temporal evolutions of HW characteristics over the period of 1861-2100, including area-aggregated (a) HWD, (b) HWF, (c) HWI, (d) HWCI, (e) PR and (f) FAR of HWs exceeding the 99% quantile of the last 200-years HI of Picontrol simulations. The thinner lines represent individual model projections, whereas the thicker lines represent multi-model averages of the RCP 2.6 and 8.5 scenarios. The historical simulations are extended to 2100 by combining the RCP 2.6 and RCP 8.5 simulations. The time series are smoothed with a 20-year running mean. The same as below.

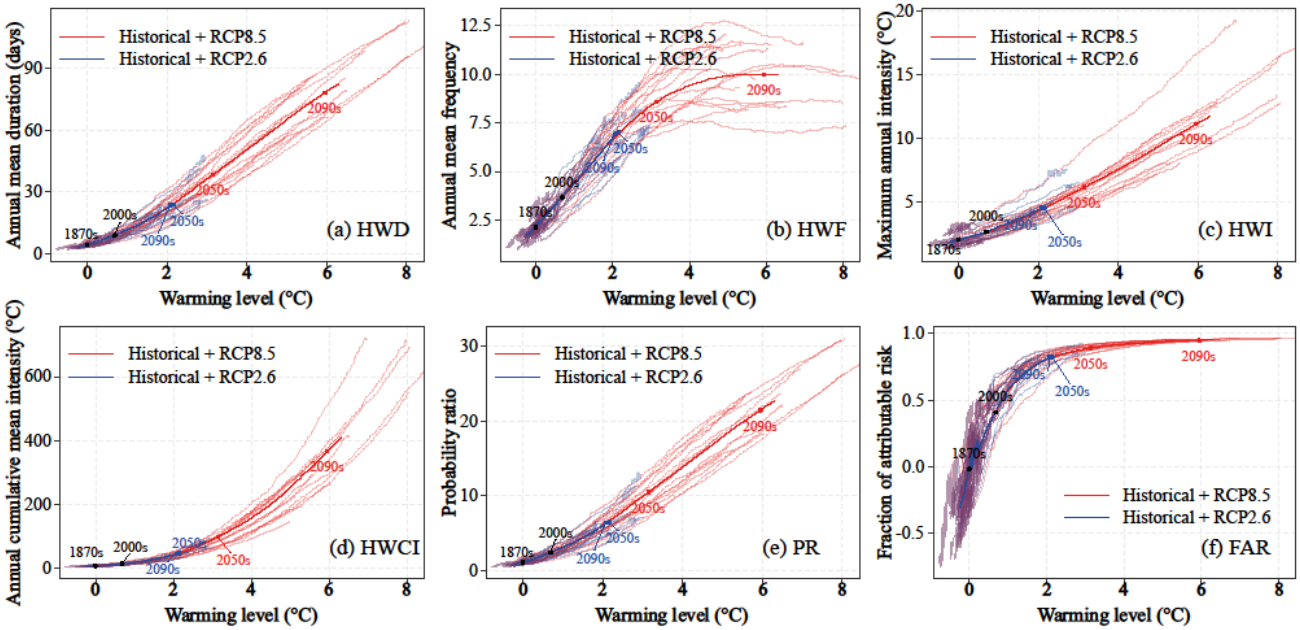

Figure 7. Simulated changes of HW characteristics for different levels of warming, including area-aggregated (a) HWD, (b) HWF, (c) HWI, (d) HWCI, (e) PR and (f) FAR of HWs exceeding the 99% quantile of the last 200-years HI of Picontrol simulations. In all panels, the simulated HW characteristics are plotted against simulated China Tmean changes relative to that of 1861–1880.

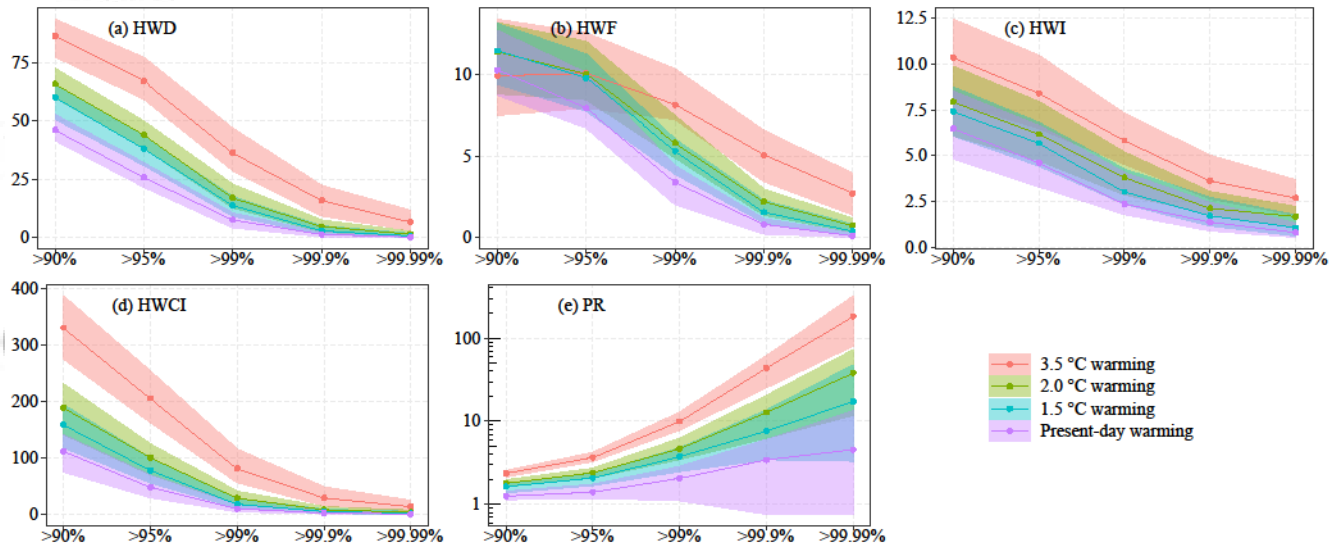

Figure 8. Simulated changes of HW characteristics for different warming levels and different thresholds. The lines represent the multi-model ensemble mean. The shading areas indicate the 5%-95% interval of individual models. Only simulations under the RCP8.5 scenario are shown here.

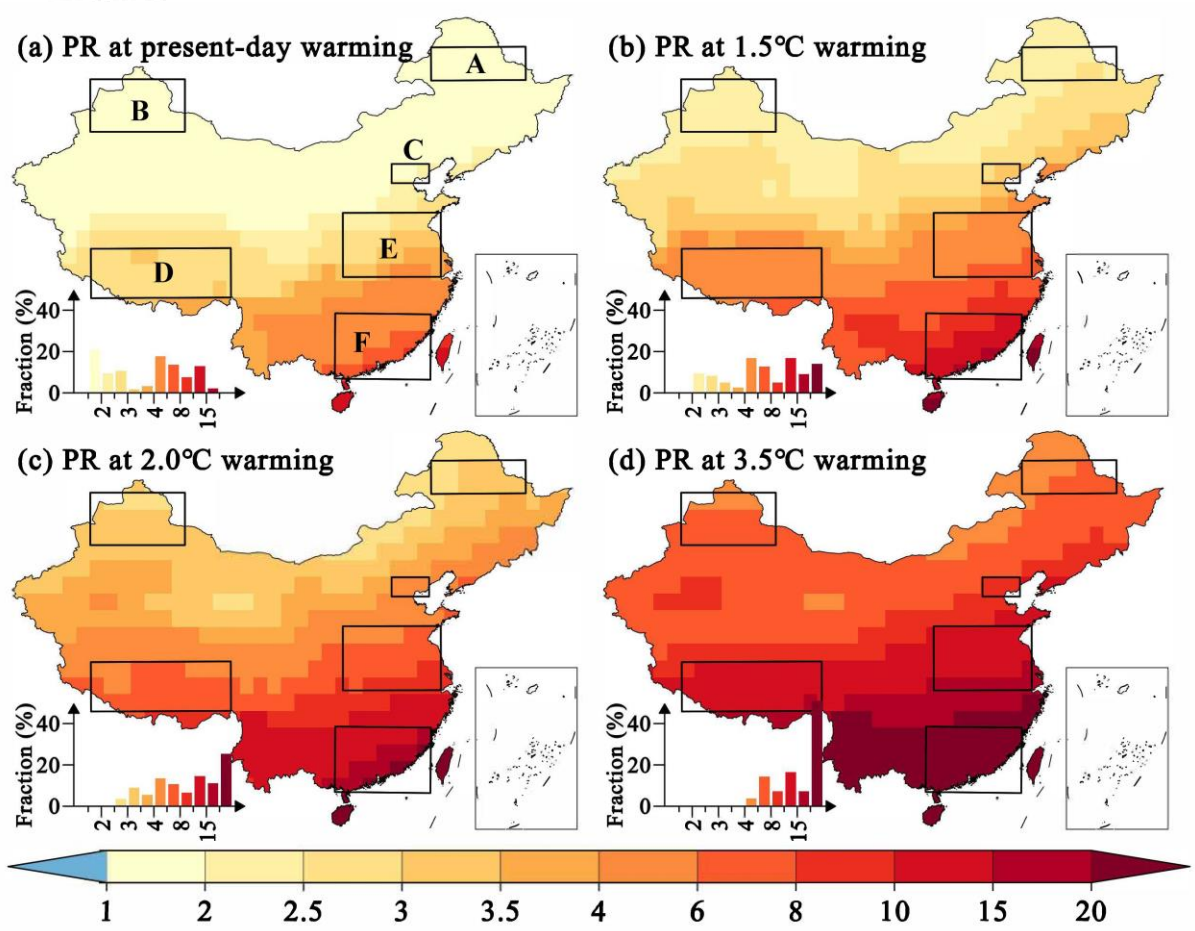

Figure 9. Spatial distribution of PR of HWs exceeding the 99% quantile of the last 200 years in Picontrol simulations at different warming levels. Six representative regions are selected to explore the temporal evolution of HWs to different levels of warming in Figure 10. A: Northeastern China, B: XinJiang, C: Beijing-Tianjin-Hebei, D: XiZang, E: Central China, F: Southern China.

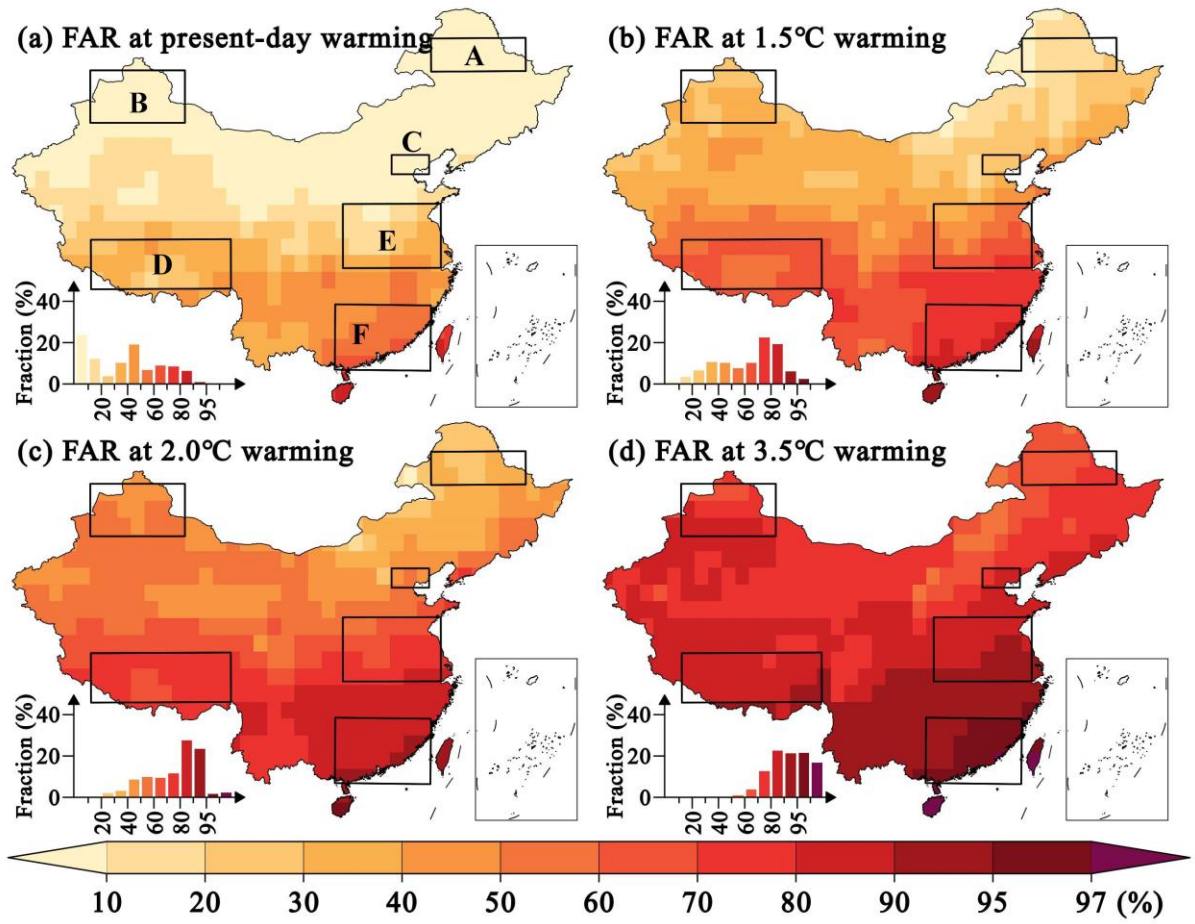

Figure 10. Spatial distribution of FAR of HWs exceeding the 99% quantile of the last 200 years in Picontrol simulations at different warming levels.

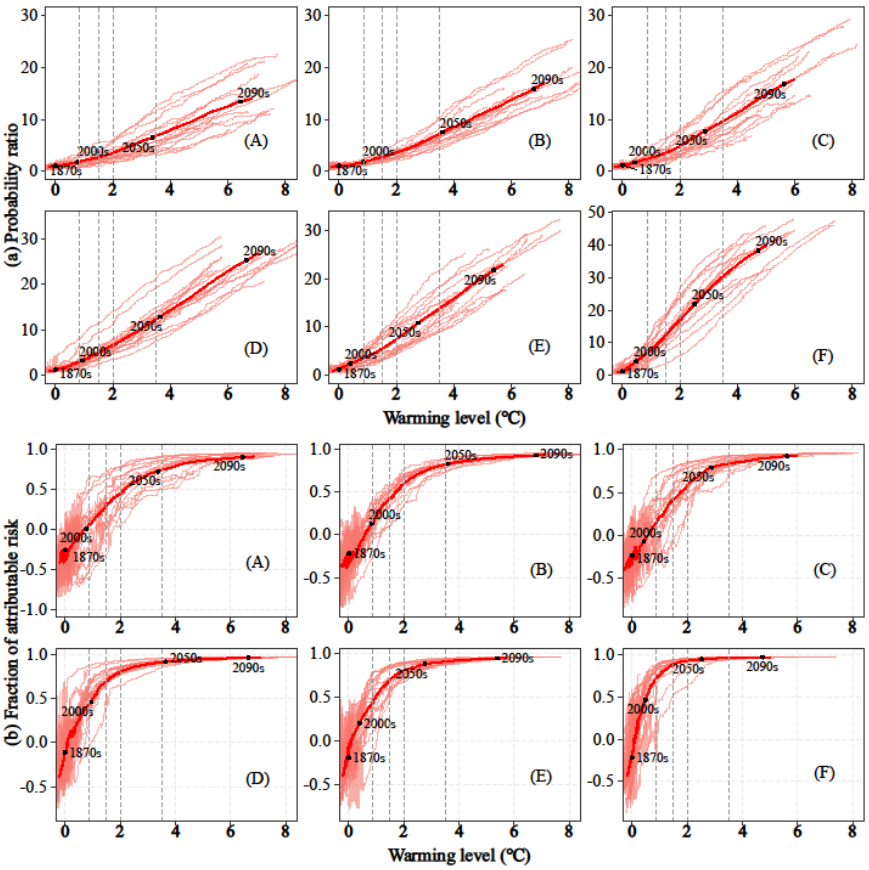

Figure 11. Simulated changes of (a) PR and (b) FAR under different levels of warming at six representative regions selected in Figure 9. The four vertical dash lines in each subplot present the present-day, 1.5℃, 2℃and 3.5℃warming levels. A: Northeastern China, B: XinJiang, C: Beijing-Tianjin-Hebei, D: XiZang, E: Central China, F: Southern China.

Tables

Table 1 List of GCMs and the number of 52-year chunks for the piControl simulations used in this study. The "piControl" row indicates the number of 52-year chunks in the corresponding GCM and the number "1" in the last three "RCP" rows indicates the simulations are available in the corresponding GCM.

Model	ALL	GHG	NAT	piControl	RCP 2.6	RCP 4.5	RCP 8.5
ACCESS1-0	1			8		1	1
ACCESS1-3	1			8		1	1
BNU-ESM	1			10	1	1	1
CNRM-CM5	1	1	1	16	1	1	
CanESM2	1	1	1	20	1	1	1
GFDL-ESM2G	1			8	1	1	1
GFDL-ESM2M	1			8	1	1	1
HadGEM2-CC	1			4		1	1
HadGEM2-ES	1			10	1	1	1
IPSL-CM5A-LR	1	1	1	18	1	1	1
IPSL-CM5A-MR	1		1	4	1	1	1
IPSL-CM5B-LR	1			4		1	1
MIROC-ESM	1			12	1	1	1

MIROC-ESM-CHEM	1			4	1	1	1
MIROC5	1			12	1	1	1
MRI-CGCM3	1			8	1	1	1
NorESM1-M	1	1	1	8	1	1	1
bcc-csm1-1	1	1	1	8	1	1	1
bcc-csm1-1-m	1			6	1	1	1
inmcm4	1			8		1	1
Total realizations	20	5	6	184	15	20	19
Total models	20	5	6	20	15	20	19

Table 2 Simulated HWD, HWF, HWI, and HWCI of human-perceived HWs exceeding the preindustrial 99th percentile over China for different warming levels.

Warming (°C)	**HWD (days)**	**HWF**	**HWI (°C)**	**HWCI (°C)**
0.85	9.36 (7.30, 13.20)	4.16 (2.84, 4.69)	2.68 (2.15, 3.70)	13.97 (10.29, 22.38)
1.5	15.92 (11.07, 20.80)	5.78 (4.24, 6.57)	3.46 (2.81, 4.51)	26.00 (18.51, 36.41)
2	21.60 (14.80, 29.02)	6.80 (5.22, 7.94)	4.24 (3.38, 5.14)	41.07 (27.55, 52.97)
3.5	43.63 (32.29, 54.53)	8.91 (7.39, 11.08)	6.69 (5.15, 8.03)	117.28 (80.37, 146.16)

Note: Multi-ensemble mean estimates are shown, and the associated 5%-95 interval of model estimates are given in parenthesis.

Table 3 Simulated PR and FAR over China for different warming levels and different preindustrial thresholds (99^{th} and 99.99^{th} percentiles).

Warming (°C)	99^{th} percentile		99.99^{th} percentile	
	PR	**FAR**	**PR**	**FAR**
0.85	2.56 (2.00, 3.65)	0.53 (0.35, 0.68)	12.15 (5.05, 22.01)	0.77 (0.51, 0.89)
1.5	4.36 (3.03, 5.70)	0.75 (0.61, 0.81)	34.38 (13.37, 65.11)	0.95 (0.80, 0.97)
2	5.92 (4.05, 7.95)	0.82 (0.73, 0.87)	64.54 (21.30, 119.05)	0.98 (0.89, 0.99)
3.5	11.95 (8.84, 14.94)	0.91 (0.88, 0.93)	300.22 (106.00, 486.78)	1.00 (0.98, 1.00)

Note: Multi-ensemble mean estimates are shown, and the associated 5%-95 interval of model estimates are given in parenthesis.